

Damage Vision Mining Opportunity for Imbalanced Anomaly Detection

Takato Yasuno

yasunotkt@gmail.com

Abstract

In past decade, previous balanced datasets have been used to advance algorithms for classification, object detection, semantic segmentation, and anomaly detection in industrial applications. Specifically, for condition-based maintenance, automating visual inspection is crucial to ensure high quality. Deterioration prognostic attempts to optimize the fine decision process for predictive maintenance and proactive repair. In civil infrastructure and living environment, damage data mining cannot avoid the imbalanced data issue because of rare unseen events and high quality status by improved operations. For visual inspection, deteriorated class acquired from the surface of concrete and steel components are occasionally imbalanced. From numerous related surveys, we summarize that imbalanced data problems can be categorized into four types; 1) missing range of target and label valubables, 2) majority-minority class imbalance, 3) foreground-background of spatial imbalance, 4) long-tailed class of pixel-wise imbalance. Since 2015, there has been many imbalanced studies using deep learning approaches that includes regression, image classification, object detection, semantic segmentation. However, anomaly detection for imbalanced data is not yet well known. In the study, we highlight one-class anomaly detection application whether anomalous class or not, and demonstrate clear examples on imbalanced vision datasets: blood smear, lung infection, hazardous driving, wooden, concrete deterioration, river sludge, and disaster damage. Illustrated in Figure 1, we provide key results on damage vision mining advantage, hypothesizing that the more effective range of positive ratio, the higher accuracy gain of anomaly detection application. In our imbalanced studies, compared with the balanced case of positive ratio 1/1, we find that there is applicable positive ratio 1/8, where the accuracy are consistently high. However, extremely imbalanced range from 1/128 to 1/16, whose accuracy are inferior to those of applicable ratio. In contrast, ranged with positive ratio over 1/4, it is shifting in over-mining phase without effective gain of accuracy. Finally, limitations and future works are mentioned.

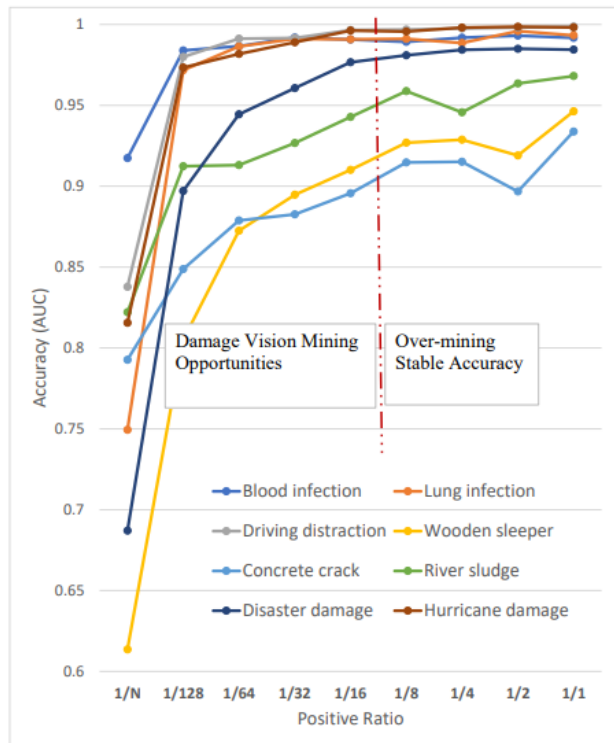


Figure 1. Illustration of damage vision mining processing on the positive ratio of target anomalous class in imbalanced datasets.

1. Introduction

1.1. Related Works for Imbalanced Vision Data

1.1.1 Imbalanced Regression

In the study, we reviewed previous machine learning approach toward imbalanced data. As shown in Table 1, we pointed out the imbalanced settings and unbiased technique examples. Regarding the imbalanced regression, Yang et al. defined Deep Imbalanced Regression (DIR) dealing with potential missing data for continuous target values, and the *distribution smoothing* techniques for both labels and features were presented [38], illustrated in Figure 2. The smoothing regression techniques were applied to five datasets with the missing value range such as age, cate-

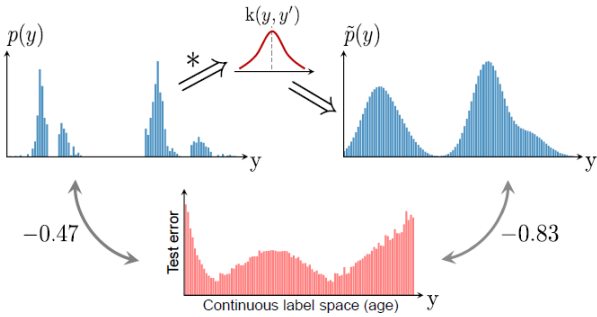


Figure 2. Imbalanced regression: e.g. Label distribution smoothing using a symmetric kernel (Yang et al. 2021).

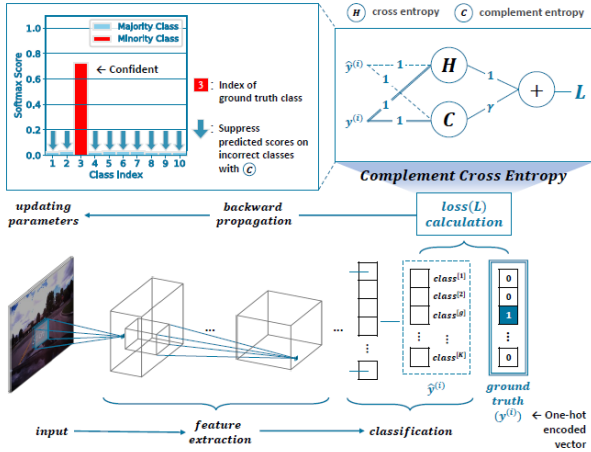


Figure 3. Imbalanced image classification: e.g. Complement cross entropy (Kim et al. 2020).

gorical label, and health score. Stocksieker et al. presented a data augmentation (DA) algorithm that combines a weighted resampling (WR) and a DA procedure [32]. Using Generalized Additive Models under synthetic data generators, six DA approaches were compared such as Gaussian noise, smoothed bootstrap, k-Nearest Neighbors, Gaussian Mixture Models, and Gaussian Coupula. However, the effect of the mean square error using DA-WR approach were dependent on the choice of the imbalanced data generator, and any DA technique had not been clearly found to improve imbalanced regression.

1.1.2 Imbalanced Image Classification

To address imbalanced image classification between majority classes and minority classes, a previous common pre-process is resampling-based approaches to the initial setting dataset. These are categorized into synthetic oversampling from minority classes [10, 26], undersampling on majority classes [17], and a combination of both [3, 58]. Another loss function-based approach is to employ cost sensitive learning, such as reweighting sample-wise loss by in-

verse class frequency and by assigning relatively higher loss [20, 35]. In addition, Chen et al. represented the *complement cross entropy* (CCE) [6, 16], illustrated in Figure 3. The CCE is evenly suppressing softmax probabilities on incorrect classes during training, and demonstrated the efficacy. However, it has a limitation which induces a complement training time approximately two times longer because of twice back-propagation per each iteration.

In medical image classification, Kieu et al. provided a survey of deep learning for lung disease detection [15]. They discussed data imbalance as an issue and future direction of lung disease detection using deep learning. When training image classification, if the number of samples of one class is extremely higher than the other class, the resulting model would be biased. It is better to have the balanced number of images in each class. However, lung disease is relatively rare events that is not the balanced case. Under an initial phase of insufficient infection vision mining, when learning a multi-class classification of COVID-19, pneumonia and normal lungs, the number of images for pneumonia far exceeded the number of unseen infection images. After lots of pandemic experience and international collaboration in medical doctors, the COVID-19 radiography database [11] has been updated, so that the 3616 positive images of COVID-19 in chest X-ray are publicly available [14]. In the study, we present ablation studies on imbalanced positive ratio in the lung infection dataset that includes several small ratio of COVID-19 anomalies and normal images.

1.1.3 Imbalanced Object Detection

Since 2015, comprehensive object detection surveys [59, 1] have been provided in terms of methods for handling scale imbalance and spatial imbalance. There are also surveys on industrial domain-specific object detection, such as vehicle detection [33], pedestrian detection [8], face detection [52, 2]. Sun et al. [33] and Dollar et al. [8] cover the methods from the imbalance point of view since they present a comprehensive analysis of feature extraction methods that handle scale imbalance. Additionally, Litjens et al. [21] discuss deep learning applications to medical image analysis, that present challenges with their possible solutions including a limited exploration of the class imbalance problem.

Systematically, Oksuz et al. reviewed the object detection literature and identified eight imbalance problems [24], illustrated in Figure 4. Clearly, they grouped into four main types: *class imbalance*, *scale imbalance*, *spatial imbalance* and *objective imbalance*. First, class imbalance occurs when there is significant inequality among the number of samples pertaining to each class. Class imbalance are considered as the foreground-to-background relationship and imbalance among the foreground classes. Second, scale imbalance occurs when the objects have various scales and

Table 1. Damage learning methods and clear examples under imbalanced settings

Imbalance	Typical data	Learning method	Clear examples
Missing Class	Continuous Target, Label	Regression	Distribution Smoothing[32, 38]
Object Spatial	Majority-Minority Bounding Box	Image Classification	Resample[10, 17], Reweighting [20, 35], Complement[6]
Pixel-wise	Foreground-Background	Object Detection	Handling scale & objective imbalance[1, 24, 59]
	Long-tailed classes	Object Detection	Handling spatial imbalance[1, 24]
		Semantic Segmentation	Center Collapse, Equiangular Tight Frame [19, 55]

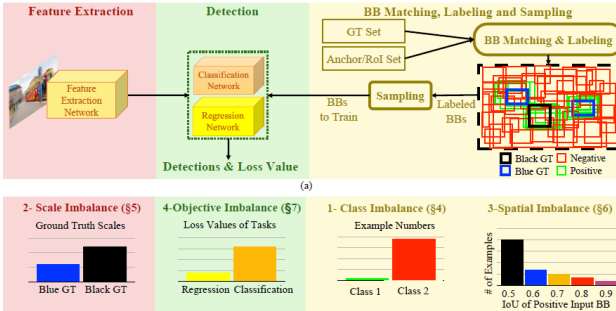


Figure 4. Imbalanced object detection: illustration of 4 imbalance categories (Oksuz et al. 2020).

numbers of samples pertaining to different scales. Third, spatial imbalance refers to a set of factors related to spatial properties of the bounding boxes such as regression penalty, location and IoU. Fourth, objective imbalance occurs when there are multiple loss functions to minimize, e.g. classification and regression losses [24].

1.1.4 Imbalanced Semantic Segmentation

Previous studies on 2D & 3D semantic segmentation mainly focused on network architecture and module design and ignored the impact of data distribution. As the datasets of semantic segmentation naturally follow a heavily imbalanced distribution among classes, neural networks perform poorly when training on them [13, 23, 28, 54]. Some studies tried to induce neural collapse in imbalanced learning for better accuracy of minor classes [34, 36, 37]. However, these studies on neural collapse are limited in recognition. As discovered by Papyan et al. [25], *neural collapse* phenomenon in that the within-class means of features and the classifier weight vectors, converge to the vertices of a *simplex equiangular tight frame* (simplex ETF) at the end of training for classification.

The simplex ETF structure in neural collapse renders feature centers equiangular separation and the maximal discriminating ability, which is able to effectively improve the performance of minor classes in long-tailed recognition [19, 57]. For understanding imbalanced semantic segmentation, the structures of feature centers and classifiers were explored by Zhong et al. [55], illustrated in Figure 5. Surprisingly, it was observed that the symmetric equiangular

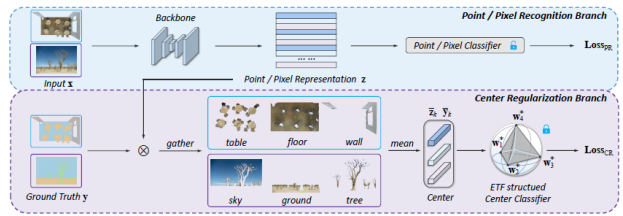


Figure 5. Imbalanced semantic segmentation: e.g. Center collapse regularizer using equiangular tight frame (Zhong et al. 2023).

separation as instructed by the neural collapse phenomenon in image recognition did not hold in semantic segmentation for both feature centers and classifiers. To take advantage of the equiangular and maximum separation properties for better performance on minor classes, the Center Collapse (CeCo) regularizer were presented for imbalanced semantic segmentation problems.

1.2. Imbalanced Anomaly Detection Application for Damage Vision Inspection

For condition-based maintenance, automating visual inspection is crucial to ensure high quality. Deterioration prognostic attempts to optimize the fine decision process for predictive maintenance and proactive repair. In civil infrastructure and living environment, damage data mining cannot avoid the imbalanced data issue because of rare unseen events and high quality status by improved operations. As shown in Table 1, we pointed out the imbalanced settings and clear examples. From aforementioned related works, we summarized that imbalanced data problems could be categorized into four types; 1) missing range of target and label values, 2) majority-minority class imbalance, 3) foreground-background of spatial imbalance, 4) long-tailed class of pixel-wise imbalance. Since 2015, there has been many imbalanced data studies based on deep learning algorithms using regression, image classification, object detection, semantic segmentation. However, anomaly detection approach for imbalanced data is not yet sufficiently known. In the present study, we propose one-class anomaly detection application whether anomalous class or not, and demonstrate clear examples on imbalanced vision datasets: wooden, concrete deterioration, and disaster damage.

The previous imbalanced studies have been based on *non-damage* vision datasets. Any damage region of interest

has been not included in the existing research scope using learning methods, e.g. regression, image classification, object detection, and semantic segmentation. In the present imbalanced studies, illustrated in the aforementioned Figure 1, we provide key results on the significance of damage vision mining, hypothesizing that the more effective ratio of anomalous class, the higher accuracy gain of anomaly detection applications. We hypothesize that the damage vision mining process is changed into significant two phases. The damage vision mining phases contains 1) *damage vision mining opportunity* the former phase with higher accuracy gain, 2) *over-mining* the latter phase without further gain of accuracy. The former phase of damage vision mining opportunity is significantly beneficial because of higher performance than the unsupervised learning without anomalous data mining, and also promising advantage of accuracy by damage vision mining.

2. Imbalanced Anomaly Detection Application

2.1. One-class Classification Using Deeper FCDDs

The authors [50] have already presented the deeper FCDDs and found the applicability to damage datasets of bridge, dam, and building. However, anomaly detection approach for imbalanced data is not yet sufficiently known. For the imbalanced studies, we summarize one-class anomaly detection method to recognize whether anomalous or normal class for applying imbalanced vision datasets.

Let I_k be the k -th image in an imbalanced vision dataset with a size of $h \times w$. We consider the number of training images and the weight W of the fully convolutional network (FCN). Let the $\Phi_W^b(I_k)$ denote a mapping of the deeper CNN to backbone b based on the input image. The one-class classification model was formulated using the cross-entropy loss function as follows:

$$\begin{aligned} \mathcal{L}_{DeepSVDD} = & -\frac{1}{n} \sum_{k=1}^n (1 - a_k) \log \ell(\Phi_W^b(I_k)) \\ & + a_k \log [1 - \ell(\Phi_W^b(I_k))], \end{aligned} \quad (1)$$

where $a_k = 1$ denotes the anomalous label of the k -th damage vision and $a_k = 0$ denotes the normal label of the k -th non-damage vision. A pseudo-Huber loss function is introduced to obtain a more robust loss formulation [30] in Equation (2). Let $\ell(u)$ be the loss function and define the pseudo-Huber loss as follows:

$$\ell(u) = \exp(-H(u)), \quad H(u) = \sqrt{\|u\|^2 + 1} - 1. \quad (2)$$

Then, a deeper FCDD loss function can be formulated :

$$\begin{aligned} \mathcal{L}_{deeperFCDD} = & \frac{1}{n} \sum_{k=1}^n \frac{(1 - a_k)}{uv} \sum_{x,y} H_{x,y}(\Phi_W^b(I_k)) \\ & - a_k \log \left[1 - \exp \left\{ \frac{-1}{uv} \sum_{x,y} H_{x,y}(\Phi_W^b(I_k)) \right\} \right], \end{aligned} \quad (3)$$

where $H_{x,y}(u)$ are the elements (x, y) of the receptive field of size $u \times v$ under a deeper FCDD. In the equation (3), if we set an unsupervised learning, the positive second term are canceled out. If we use an imbalanced vision data that includes fewer anomalous images and relatively large normal images, a deeper FCDD loss function (3) is less influenced by the positive second term. The anomaly score S_k of the k -th image is expressed as the sum of all the elements of the receptive field as follows:

$$S_k(b) = \sum_{x,y} H_{x,y}(\Phi_W^b(I_k)), \quad k = 1, \dots, n. \quad (4)$$

We herein present the construction of a baseline FCDD [50] with an initial backbone $b = 0$ and performed CNN27 mapping $\Phi_W^0(I_k)$ from the input image A_k in the imbalanced vision dataset. We also present deeper FCDDs focusing on elaborate backbones $b \in \{VGG16, ResNet101, Inceptionv3\}$ with a mapping operation $\Phi_W^b(I_k)$ to achieve more elaborately performance. In this paper, we present ablation studies on anomalous ratio of imbalanced datasets for detecting material deterioration and disaster damage.

2.2. Damage-mark Heatmap Upsampling

Convolutional neural network (CNN) architectures, comprising millions of common parameters, have exhibited remarkable performance for visual inspection, but the underlying reasons for this superiority remain unclear. Heatmap visualization techniques for detecting and localizing anomalous features are typically categorized as masked sampling and activation map approaches. The former includes methods such as occlusion sensitivity [53] and local interpretable model-agnostic explanations [29]. The latter category includes activation maps such as class activation maps (CAMs) [56] and gradient-based extensions (Grad-CAM) [31]. Nonetheless, aforementioned methods of disadvantage is its requirement for parallel computation resources and iterative computation time for local partitioning, masked sampling, and for generating a gradient-based heatmap.

In this study for anomaly detection applications, we adopt the receptive field upsampling approach [22] to visualize anomalous features using an upsampling-based activation map with Gaussian upsampling from the receptive field of the FCN. The primary advantages of the upsampling approach are the reduced computational resource requirements and shorter computation times. The proposed

upsampling algorithm generates a full-resolution anomaly heatmap from the input of a low-resolution receptive field $u \times v$.

Let $H \in R^{u \times v}$ be a low-resolution receptive field (input), and let $H' \in R^{h \times w}$ be a full-resolution of damage-mark heatmap (output). We define the 2D Gaussian distribution $G_2(m_1, m_2, \sigma)$ as follows:

$$[G_2(m_1, m_2, \sigma)]_{x,y} \equiv \frac{1}{2\pi\sigma^2} \exp\left(-\frac{(x-m_1)^2 + (y-m_2)^2}{2\sigma^2}\right). \quad (5)$$

The Gaussian upsampling algorithm from the receptive field is implemented as follows:

1. $H' \leftarrow 0 \in R^{h \times w}$
2. for all output pixels d in $H \leftarrow 0 \in R^{u \times v}$
3. $u(d) \leftarrow$ is upsampled from a receptive field of d
4. $(c_1(u), c_2(u)) \leftarrow$ is the center of the field $u(d)$
5. $H' \leftarrow H' + d \cdot G_2(c_1, c_2, \sigma)$
6. end for
7. return H'

After conducting experiments with various datasets, we determined that a receptive field size of 28×28 is a practical value. When generating a deterioration heatmap, revealed damage mark, we need to unify the display range that corresponds to the anomaly scores, which range from the minimum to the maximum value. In order to strengthen the defective regions and highlight the hazard marks, we define a display range of $[\min, \max/4]$, where the quartile parameter is 0.25. This results in the histogram of anomaly scores having a long-tailed shape. If we were to include the complete anomaly score range, the colors would weaken to blue or yellow on the maximum side.

3. Applied Results

3.1. Class Imbalanced Vision Data

In the present study, we highlighted three imbalanced datasets as shown in Table 2, the training data contains anomalous and normal images. In the present study, we implemented deeper backbone studies using the VGG16, ResNet101, Inceptionv3. During the training of the anomaly detector, we fixed the input size to 256^2 training for the wooden sleeper dataset, and to 224^2 training for concrete deterioration and disaster damage. To train the model, we set the mini-batch size to 32 and ran 60 epochs. In this study, we used the Adam optimizer with a learning rate of

0.0001, a gradient decay factor of 0.9, and a squared gradient decay factor of 0.99. The training images were partitioned at a ratio of 65:15:20 for the training, calibration, and testing images in each dataset. Herein, N_d ($d = 1, 2, 3$) denotes the number of training data in the dataset d , and M_d stands for the total number of the dataset that contains the calibration and testing images.

1. *Blood infection* $N_1 = 1300, M_1 = 2000$.
 - malaria parasitized in blood smear images by cell-level ([27]).
2. *Lung infection* $N_2 = 1300, M_2 = 2000$.
 - COVID-19 in chest X-ray images ([11, 14]).
3. *Driving distraction* $N_3 = 1300, M_3 = 2000$.
 - 4-classes : distracted driving images, i.e. texting-left and -right, talking on the phone-left and -right ([7, 12]).
4. *Wood deterioration* $N_4 = 1300, M_4 = 2000$.
 - decayed wooden sleeper in rural railway.
5. *Concrete damage* $N_5 = 1300 = 650 \times 2, M_5 = 2000$.
 - 2-classes : crack on pavement and deck (SDNET [9]).
6. *River sludge* $N_6 = 1300 = 650 \times 2, M_6 = 2000$.
 - floating sludge on the river surface images ([44]).
7. *Disaster damage* $N_7 = 1300 = 325 \times 4, M_7 = 2000$.
 - 4-classes : building collapse, flooding area, traffic incidents, fire/smoke (AIDER [18]).
8. *Hurricane damage* $N_8 = 1300, M_8 = 2000$.
 - Hurricane satellite imagery ([4, 5]).

Table 2. Imbalanced training dataset d of target damage.(Each class has N_d images in the normal and anomalous class. At least, the calibration 300 and test 400 images were fixed respectively.)

Positive ratio	Anomalous	Normal
1/1(supervised)	N_d	N_d
1/2	$N_d/2$	N_d
1/4	$N_d/4$	N_d
1/8	$N_d/8$	N_d
1/16	$N_d/16$	N_d
1/32	$N_d/32$	N_d
1/64	$N_d/64$	N_d
1/128	$N_d/128$	N_d
1/ N_d (unsupervised)	1	N_d

3.2. Blood infection

3.2.1 Backbone Studies of Supervised Detection

As shown in Table 3, our deeper FCDD-ResNet101 outperformed in terms of the F_1 , precision, and recall rather than the baseline CNN27 and other backbone-based deeper FCDDs in this blood smear images dataset for detecting malaria parasitized cells.

Table 3. Backbone ablation studies on malaria parasitized cells detection using our proposed deeper FCDDs.

Backbone	AUC	F_1	Precision	Recall
CNN27	0.9853	0.9468	0.9589	0.9350
VGG16	0.9932	0.9689	0.9629	0.9750
ResNet101	0.9917	0.9774	0.9799	0.9750
Inceptionv3	0.9913	0.9759	0.9872	0.9650

3.2.2 Imbalanced-to-unsupervised Training Results

As shown in Table 4, we implemented ablation studies on imbalanced data that contains smaller anomalous images and relatively large normal images. Herein, we applied our deeper FCDD-ResNet101 achieved high performance in the aforementioned supervised results. Compared with the balanced case of positive ratio 1/1, we found that there was applicable range from the imbalanced ratio 1/2 to the ratio 1/16 where the accuracy of recall was consistently less than 4%. However, extremely imbalanced range from 1/32 to 1/1300, that accuracy were inferior to those of applicable range, e.g. the recall was more than 5%. The rare positive ratio 1/32 represent the imbalanced data that contains quite a little 41 anomalous images and relatively large 1300 normal images. In the situation, much more anomalous images should be acquired and added to the initial dataset. The marginal gain of accuracy was relatively high by adding the blood infection images of malaria parasitized cells.

Table 4. Imbalanced data studies using our deeper FCDD-ResNet101 for Blood infection detection $N_1 = 1300$.

Positive ratio	AUC	F_1	Precision	Recall
1/1(ano.N_1)	0.9917	0.9774	0.9799	0.9750
1/2(ano.650)	0.9931	0.9735	0.9797	0.9675
1/4(ano.325)	0.9918	0.9683	0.9820	0.9550
1/8(ano.163)	0.9893	0.9660	0.9721	0.9600
1/16(ano.81)	0.9907	0.9636	0.9672	0.9600
1/32(ano.41)	0.9919	0.9619	0.9768	0.9475
1/64(ano.20)	0.9866	0.9532	0.9641	0.9425
1/128(ano.10)	0.9839	0.9590	0.9816	0.9375
1/N_1(ano.1)	0.9174	0.8239	0.8610	0.7900

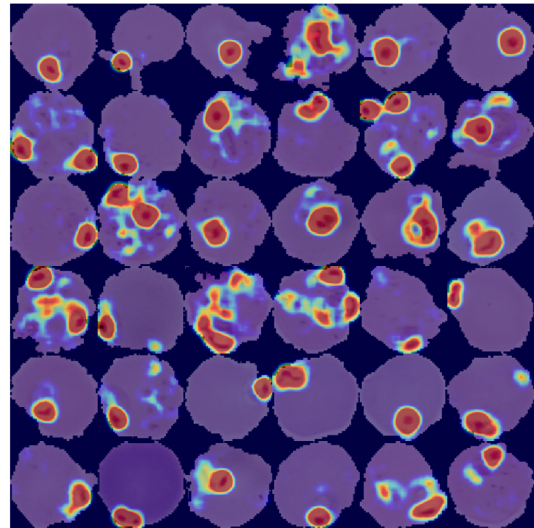
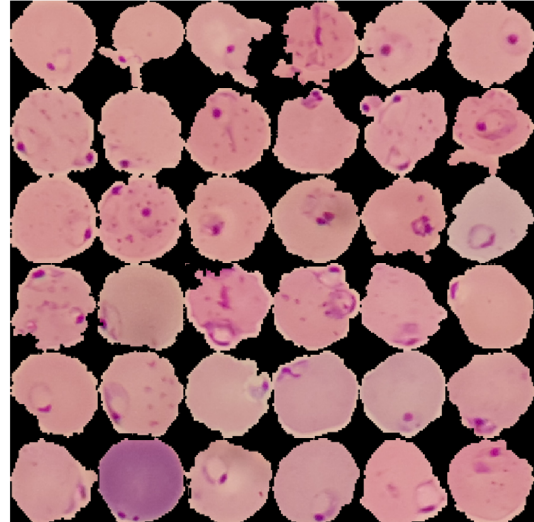


Figure 6. Imbalanced damage images (top) with positive ratio 1/16, and damage-mark heatmaps (bottom) of blood infection using our deeper FCDD-ResNet101.

3.2.3 Damage-mark Heatmaps on Blood Infection

We visualized the damage features by using Gaussian up-sampling in our deeper FCDD-ResNet101 network. Additionally, we generated a histogram of the anomaly scores of the test images in the imbalanced case with positive ratio 1/16. In Fig. 6, a damage-mark explanation is represented. The red region in the heatmap represents the malaria parasitized cells of features in the blood smear images. Fig. 7 illustrates that a few overlapping bins exist in the boundary of the uninfected class and malaria parasitized class along the horizontal anomaly scores. Thus, for detecting malaria parasitized cells, the score range was well separated in the

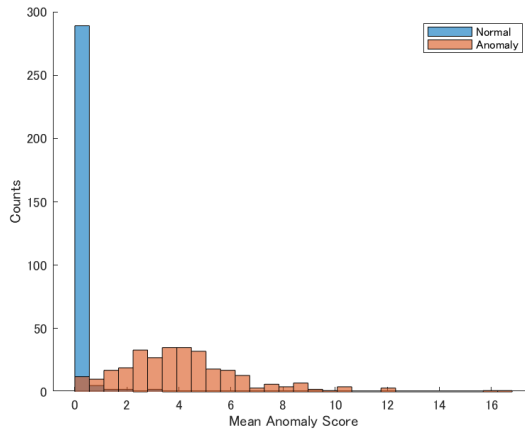


Figure 7. Histogram of blood infection scores using our deeper FCDD-ResNet101 corresponding to the imbalanced damage images with positive ratio 1/16.

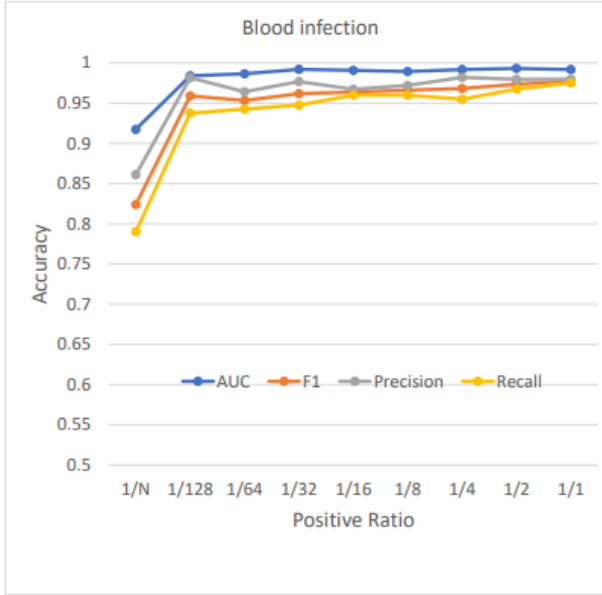


Figure 8. Anomalous vision mining studies on blood infection, indicates that the more anomalies of damage vision, the higher performance of anomaly detection.

blood smear images dataset.

3.2.4 Effect on Damage Class Mining

As shown in Figure 8, from the view point of all accuracy, the imbalanced studies on blood infection implied that all of accuracy were consistently converged into significant phases. Ranged with the positive ratio less than 1/8, we could understand that there were damage vision mining opportunities with accuracy gain in terms of the AUC. In contrast, ranged with positive ratio over 1/4, it was shifting in

over-mining phase without any gain of the AUC. The former phase of damage vision mining opportunities has become beneficial because of promising advantage of higher accuracy in all of them.

3.3 Lung infection

3.3.1 Backbone Studies of Supervised Detection

As shown in Table 5, our deeper FCDD-ResNet101 outperformed in terms of the F_1 , precision, and recall rather than the baseline CNN27 and other backbone-based deeper FCDDs in this chest X-ray images dataset for detecting lung infection of COVID-19.

Table 5. Backbone ablation studies on lung infection detection using our proposed deeper FCDDs.

Backbone	AUC	F_1	Precision	Recall
CNN27	0.9359	0.8677	0.8095	0.9350
VGG16	0.9925	0.9662	0.9674	0.9650
ResNet101	0.9933	0.9725	0.9701	0.9750
Inceptionv3	0.9918	0.9576	0.9552	0.9600

3.3.2 Imbalanced-to-unsupervised Training Results

As shown in Table 6, we implemented ablation studies on imbalanced data that contains smaller anomalous images and relatively large normal images. Herein, we applied our deeper FCDD-ResNet101 achieved high performance in the aforementioned supervised results. Compared with the balanced case of positive ratio 1/1, we found that there was applicable range from the imbalanced ratio 1/2 to the ratio 1/16 where the accuracy of F_1 was consistently more than 95%. However, extremely imbalanced range from 1/32 to 1/1300, that accuracy were inferior to those of applicable range, e.g. the F_1 was more than 95%. The rare positive ratio 1/32 represent the imbalanced data that contains quite a little 41 anomalous images and relatively large 1300 normal images. In the situation, much more anomalous images should be acquired and added to the initial dataset. The marginal gain of accuracy was relatively high by adding the lung infection images of COVID-19.

3.3.3 Damage-mark Heatmaps on Lung Infection

We visualized the damage features by using Gaussian up-sampling in our deeper FCDD-ResNet101 network. Additionally, we generated a histogram of the anomaly scores of the test images in the imbalanced case with positive ratio 1/16. In Fig. 9, a damage-mark explanation is represented. The red region in the heatmap represents the COVID-19 lung infection of features in the chest X-ray images. Fig. 10 illustrates that a few overlapping bins exist in the boundary of the normal class and COVID-19 infected class along the

Table 6. Imbalanced data studies using our deeper FCDD-ResNet101 for Lung infection detection $N_2 = 1300$.

Positive ratio	AUC	F_1	Precision	Recall
1/1(ano. N_2)	0.9933	0.9725	0.9701	0.9750
1/2(ano.650)	0.9959	0.9764	0.9680	0.9850
1/4(ano.325)	0.9885	0.9650	0.9650	0.9650
1/8(ano.163)	0.9911	0.9527	0.9738	0.9325
1/16(ano.81)	0.9908	0.9533	0.9618	0.9450
1/32(ano.41)	0.9911	0.9404	0.9148	0.9675
1/64(ano.20)	0.9864	0.9468	0.9589	0.9350
1/128(ano.10)	0.9717	0.9154	0.9108	0.9200
1/N_2(ano.1)	0.7494	0.7088	0.7027	0.7150

horizontal anomaly scores. Thus, for detecting lung infection of the COVID-19, the score range was well separated in the chest X-ray images dataset.

3.3.4 Effect on Damage Class Mining

As shown in Figure 11, from the view point of all accuracy, the imbalanced studies on lung infection implied that all of accuracy were consistently converged into significant phases. Ranged with the positive ratio less than 1/8, we could understand that there were damage vision mining opportunities with accuracy gain in terms of the AUC. In contrast, ranged with positive ratio over 1/4, it was shifting in over-mining phase without any gain of the AUC. The former phase of damage vision mining opportunities has become beneficial because of promising advantage of higher accuracy in all of them.

3.4. Driving Distraction

3.4.1 Backbone Studies of Supervised Detection

As shown in Table 7, our deeper FCDD-Inceptionv3 outperformed in terms of the F_1 , precision, and recall rather than the baseline CNN27 and other backbone-based deeper FCDDs in this driving distraction images dataset for detecting hazardous driving behaviors.

Table 7. Backbone ablation studies on distracted driving detection using our proposed deeper FCDDs.

Backbone	AUC	F_1	Precision	Recall
CNN27	0.9445	0.8894	0.8839	0.8950
VGG16	0.9981	0.9937	0.9949	0.9925
ResNet101	0.9955	0.9836	0.9923	0.9750
Inceptionv3	0.9987	0.9974	1.000	0.9950

3.4.2 Imbalanced-to-unsupervised Training Results

As shown in Table 8, we implemented ablation studies on imbalanced data that contains smaller anomalous images and relatively large normal images. Herein, we applied

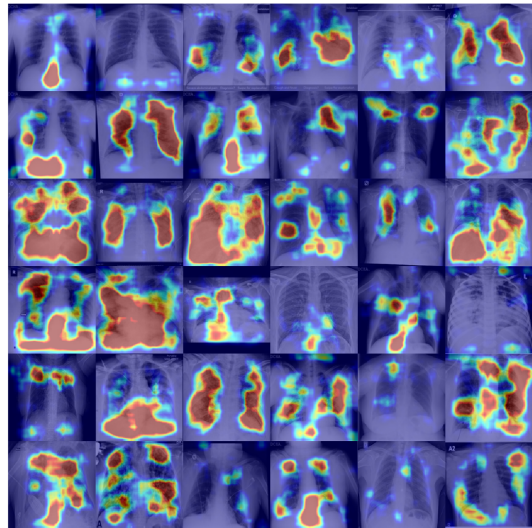
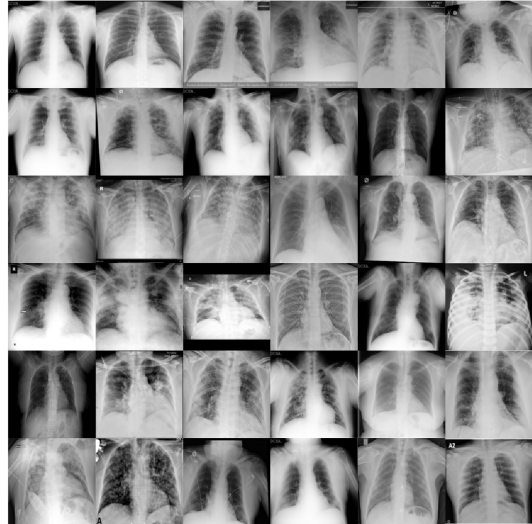


Figure 9. Imbalanced damage images (top) with positive ratio 1/16, and damage-mark heatmaps (bottom) of lung infection using our deeper FCDD-ResNet101.

our deeper FCDD-Inceptionv3 achieved high performance in the aforementioned supervised results. Compared with the balanced case of positive ratio 1/1, we found that there was applicable range from the imbalanced ratio 1/2 to the ratio 1/16 where the accuracy loss of recall was consistently less than 3%. However, extremely imbalanced range from 1/32 to 1/1300, that accuracy were inferior to those of applicable range, e.g. the loss of F_1 was more than 3%. The rare positive ratio 1/32 represent the imbalanced data that contains quite a little 41 anomalous images and relatively large 1300 normal images. In the situation, much more anomalous images should be acquired and added to the ini-

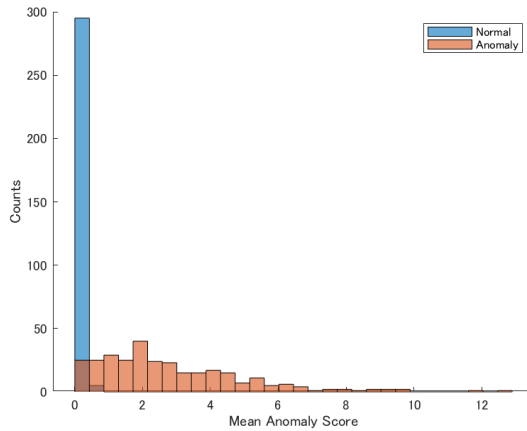


Figure 10. Histogram of lung infection scores using our deeper FCDD-ResNet101 corresponding to the imbalanced damage images with positive ratio 1/16.

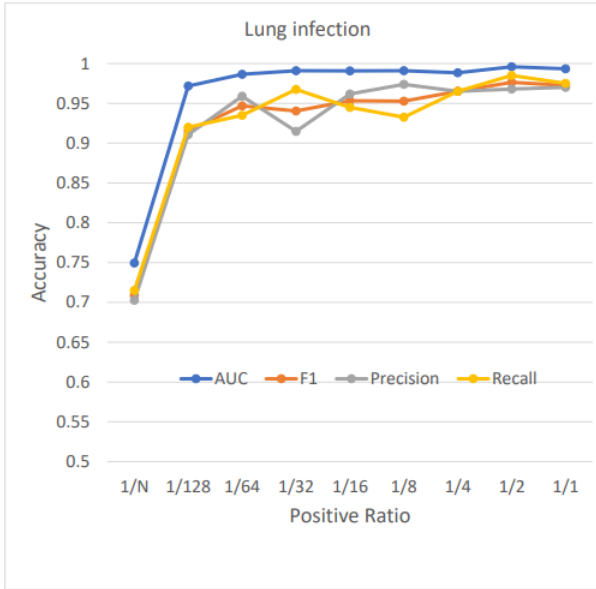


Figure 11. Anomalous vision mining studies on lung infection, indicates that the more anomalies of damage vision, the higher performance of anomaly detection.

tial dataset. The marginal gain of accuracy was relatively high by adding the driving distraction images of texting and talking on the phone.

3.4.3 Damage-mark Heatmaps on Driving Distraction

We visualized the damage features by using Gaussian up-sampling in our deeper FCDD-Inceptionv3 network. Additionally, we generated a histogram of the anomaly scores of the test images in the imbalanced case with positive ratio 1/16. In Fig. 12, a damage-mark explanation is repre-

Table 8. Imbalanced data studies using our deeper FCDD-Inceptionv3 for Driving distraction detection $N_3 = 1300$.

Positive ratio	AUC	F_1	Precision	Recall
1/1(ano. N_3)	0.9987	0.9974	1.000	0.9950
1/2(ano.650)	0.9981	0.9886	1.000	0.9775
1/4(ano.325)	0.9976	0.9782	1.000	0.9575
1/8(ano.163)	0.9968	0.9899	0.9949	0.9850
1/16(ano.81)	0.9965	0.9850	0.9850	0.9850
1/32(ano.41)	0.9916	0.9664	0.9604	0.9725
1/64(ano.20)	0.9912	0.9542	0.9715	0.9375
1/128(ano.10)	0.9799	0.9107	0.9437	0.8800
1/N_3(ano.1)	0.8378	0.7450	0.6971	0.8000

sented. The red region in the heatmap represents the distracted driving features that the driver behaves with one hand, while texting and talking on the phone without holding the handle by another hand. These heatmaps have focused on the anomalous hand moving as one of distracted driving behaviors that could potentially occur traffic incident. Fig. 13 illustrates that a few overlapping bins exist in the boundary of the safety driving class and distracted class along the horizontal anomaly scores. Thus, for detecting distracted driving behaviors, the score range was well separated in the blood smear images dataset.

3.4.4 Effect on Damage Class Mining

As shown in Figure 14, from the view point of all accuracy, the imbalanced studies on driving distraction implied that all of accuracy were consistently converged into significant phases. Ranged with the positive ratio less than 1/8, we could understand that there were damage vision mining opportunities with accuracy gain in terms of the AUC. In contrast, ranged with positive ratio over 1/4, it was shifting in over-mining phase without any gain of the AUC. The former phase of damage vision mining opportunities has become beneficial because of promising advantage of higher accuracy in all of them.

3.5 Wooden Deterioration

3.5.1 Backbone Studies of Supervised Detection

The number of training images N_3 in each class is 1300, and the number for calibration and test are 300 and 400 images respectively on the dataset of wooden sleeper deterioration. As shown in Table 9, our deeper FCDDs based on VGG16 (abbreviated as *deeperFCDD-VGG16*) outperformed in terms of the AUC and F_1 rather than the baseline CNN27 and other backbone-based deeper FCDDs in this railway dataset for detecting decayed wooden sleeper.

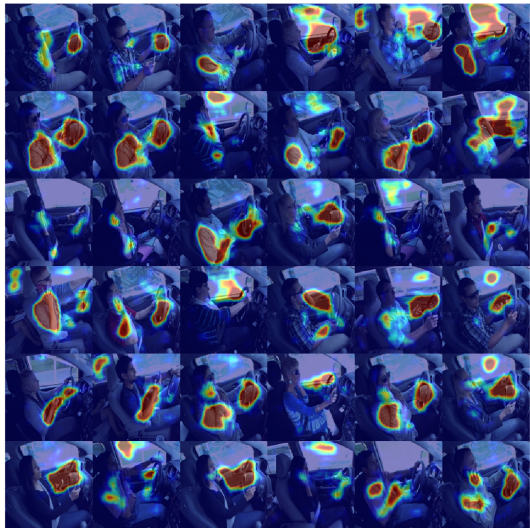


Figure 12. Imbalanced damage images (top) with positive ratio 1/16, and damage-mark heatmaps (bottom) of distracted driving using our deeper FCDD-Inceptionv3.

Table 9. Backbone ablation studies on defective detection using our proposed deeper FCDDs for Wooden sleeper.

Backbone	AUC	F_1	Precision	Recall
CNN27	0.8624	0.7688	0.7088	0.8400
VGG16	0.9425	0.8475	0.8770	0.8200
ResNet101	0.9304	0.8108	0.8823	0.7500
Inceptionv3	0.9412	0.8041	0.8415	0.7700

3.5.2 Imbalanced-to-unsupervised Training Results

As shown in Table 10, we implemented ablation studies on imbalanced data that contains fewer anomalous images and relatively large normal images. Herein, we applied our

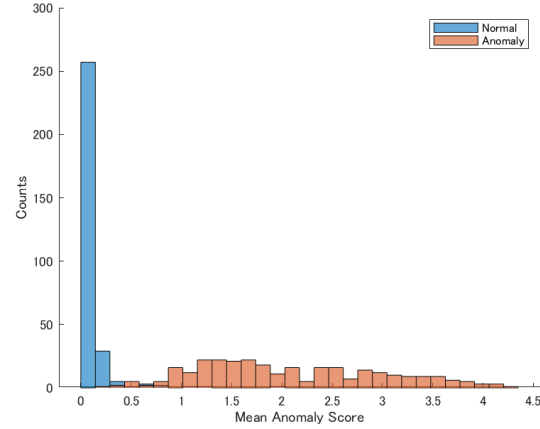


Figure 13. Histogram of distracted driving scores using our deeper FCDD-Inceptionv3 corresponding to the imbalanced damage images with positive ratio 1/16.

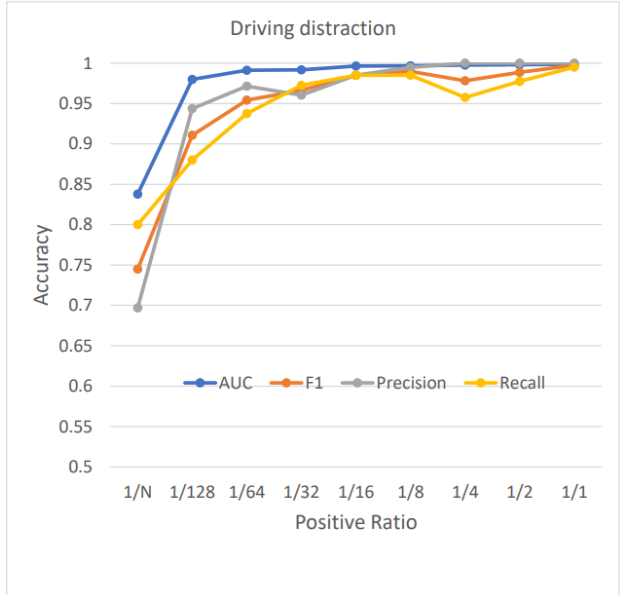


Figure 14. Anomalous vision mining studies on driving distraction, indicates that the more anomalies of damage vision, the higher performance of anomaly detection.

deeper FCDD-VGG16 achieved high performance in the aforementioned results. Compared with the balanced case of positive ratio 1/1, we found that there was applicable range from the balanced ratio 1/2 to the ratio 1/16 where every accuracy were consistently high performance. However, extremely imbalanced range from 1/32 to 1/128 and 1/1300, that accuracy were significantly decreasing and inferior to those of the applicable range. Specifically, the rare positive ratio 1/32 represent the imbalanced data that contains quite a few 41 anomalous images and relatively large 1300 normal images. In the situation, much more anomalous im-



Figure 15. Imbalanced deterioration images (top) with positive ratio 1/16, and damage-mark heatmaps (bottom) of decayed wooden sleeper using our deeper FCDD-VGG16.

ages should be acquired and added to the initial dataset. The marginal effect of accuracy gain was significantly high by adding the anomalous images.

3.5.3 Damage-mark Heatmaps on Wooden Decayed

We visualized the damage features by using Gaussian up-sampling in our deeper FCDD-VGG16 network. Additionally, we generated a histogram of the anomaly scores of the test images in the imbalanced case with positive ratio 1/16. In the bottom of Fig. 15, a damage-mark explanation is presented. The red region in the heatmap represents the

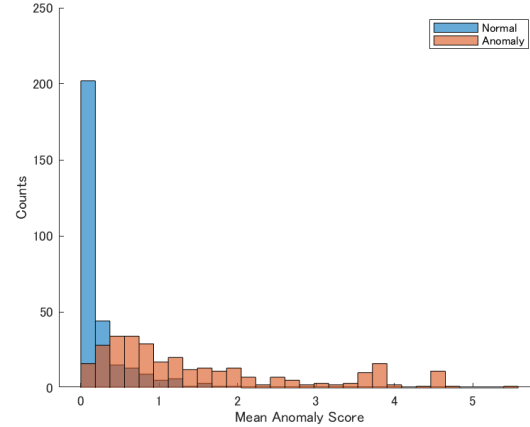


Figure 16. Histogram of decayed wooden sleeper scores using our deeper FCDD-VGG16 corresponding to the imbalanced deterioration images with positive ratio 1/16.

Table 10. Imbalanced data studies using our deeper FCDD-VGG16 for wooden sleeper deterioration $N_3 = 1300$.

Positive ratio	AUC	F_1	Precision	Recall
1/1(ano.N_3)	0.9463	0.8701	0.8379	0.9050
1/2(ano.650)	0.9190	0.8751	0.8205	0.9375
1/4(ano.325)	0.9287	0.8505	0.8274	0.8750
1/8(ano.163)	0.9269	0.8451	0.8378	0.8525
1/16(ano.81)	0.9101	0.8547	0.8353	0.8750
1/32(ano.41)	0.8947	0.8441	0.8110	0.8800
1/64(ano.20)	0.8724	0.8250	0.7562	0.9075
1/128(ano.10)	0.8051	0.7698	0.7622	0.7775
1/N_3(ano.1)	0.6136	0.5823	0.5724	0.5925

decayed wooden sleepers. There is quite a few region of background noise over the ballast stones, and precast concrete white sleeper in the third and fourth rows, and grass outside rail track in the sixth row. In addition, Fig. 16 illustrates that several overlapping bins exist in the boundary of horizontal anomaly scores between the non-damage class and deterioration class. Therefore, for detecting decayed wooden sleepers, the anomaly score range was moderately separated in the wooden sleeper deterioration dataset.

3.5.4 Effect on Deterioration Class Mining

As shown in Figure 17, from the view point of accuracy on the AUC, the imbalanced studies on wooden sleeper deterioration implied that the accuracy were moving into stable phases, even though the recall and precision were waving. Ranged with the positive ratio less than 1/8, we could understand that there were damage vision mining opportunities with accuracy gain. In contrast, ranged with positive ratio over 1/4, it was shifting in over-mining phase without effective gain of accuracy. The former phase of damage vi-

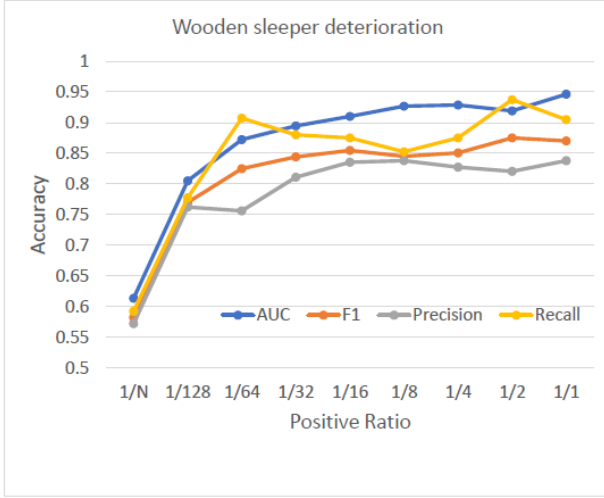


Figure 17. Anomalous vision mining studies on wooden sleeper deterioration, indicates that the more anomalies of damage vision, the higher performance of anomaly detection.

sion mining opportunities has become beneficial because of advantage of higher accuracy in terms of the AUC.

3.6. Concrete Crack

3.6.1 Backbone Studies of Supervised Detection

As shown in Table 11, our deeper FCDD-VGG16 outperformed in terms of all of accuracy, such as the AUC, F_1 , precision, and recall, rather than those of the baseline CNN27 and other backbone-based deeper FCDDs in this concrete deterioration dataset for detecting crack.

Table 11. Backbone ablation studies on concrete crack detection using our proposed deeper FCDDs.

Backbone	AUC	F_1	Precision	Recall
CNN27	0.7150	0.6975	0.6245	0.7900
VGG16	0.9287	0.8384	0.8605	0.8175
ResNet101	0.9120	0.8206	0.8480	0.7950
Inceptionv3	0.9119	0.8169	0.8372	0.7975

3.6.2 Imbalanced-to-unsupervised Training Results

As shown in Table 12, we carried out ablation studies on imbalanced damage data that contains fewer anomalous images and relatively large normal images. Herein, we applied our deeper FCDD-VGG16 achieved high performance in the above supervised results. Compared with the balanced case of positive ratio 1/1, we found that there was applicable range from the balanced ratio 1/2 to the ratio 1/8 where the accuracy were consistently high performance in terms of the AUC and F_1 . However, extremely imbalanced range from 1/16 to 1/1300, that accuracy were inferior to those

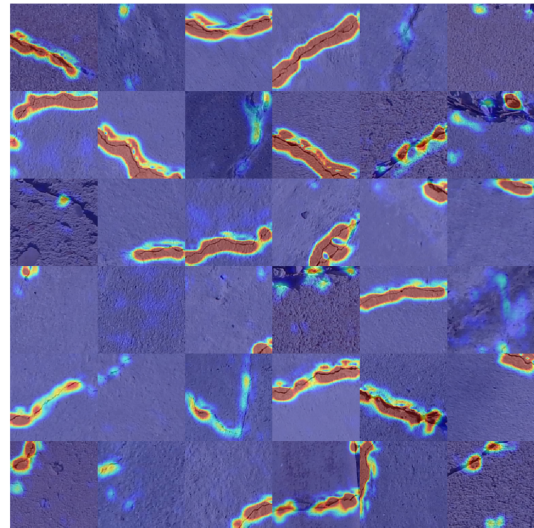


Figure 18. Imbalanced deterioration images (top) with positive ratio 1/8, and damage-mark heatmaps (bottom) of concrete crack using our deeper FCDD-VGG16.

of aforementioned applicable range. The rare positive ratio 1/16 represent the imbalanced data that contains a little 81 anomalous images and relatively large 1300 normal images. In the situation, much more anomalous images should be acquired and added to the initial dataset. The marginal gain of accuracy was relatively high by adding the deterioration images.

3.6.3 Damage-mark Heatmaps on Concrete Crack

We visualized the damage features by using Gaussian up-sampling in our deeper FCDD-VGG16 network. Additionally, we generated a histogram of the anomaly scores of the

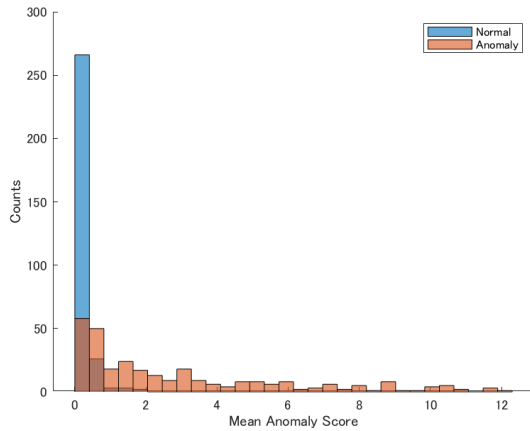


Figure 19. Histogram of concrete crack scores using our deeper FCDD-VGG16 corresponding to the imbalanced deterioration images with positive ratio 1/8.

Table 12. Imbalanced data studies using our deeper FCDD-VGG16 for Concrete crack detection $N_4 = 1300$.

Positive ratio	AUC	F_1	Precision	Recall
1/1(ano. N_4)	0.9338	0.8265	0.9482	0.7325
1/2(ano.650)	0.8968	0.8492	0.9016	0.8025
1/4(ano.325)	0.9151	0.8151	0.8856	0.7550
1/8(ano.163)	0.9147	0.8178	0.8885	0.7575
1/16(ano.81)	0.8956	0.7918	0.8594	0.7750
1/32(ano.41)	0.8826	0.7918	0.8617	0.7325
1/64(ano.20)	0.8788	0.7614	0.8952	0.6625
1/128(ano.10)	0.8488	0.7104	0.8277	0.6225
1/N_4(ano.1)	0.7927	0.6908	0.8235	0.5950

test images in the balanced case. In the bottom of Fig. 18, a damage-mark explanation is presented. The red region in the heatmap represents the crack in the surface of concrete deck and pavement. All of cracks with small width are localized sufficiently. In addition, Fig. 19 illustrates that a few overlapping bins exist in the boundary of horizontal anomaly scores between the health class and crack deterioration class. Therefore, for detecting concrete crack, the score range was well separated in the imbalanced crack dataset.

3.6.4 Effect on Deterioration Class Mining

As shown in Figure 20, from the view point of the primary accuracy AUC, the imbalanced studies on concrete crack implied that the accuracy was increasing within the range less than the positive ratio 1/8, although the precision and recall were waving. We could understand that the beneficial range was damage vision mining opportunities with accuracy gain. In contrast, ranged with positive ratio over 1/4, it was shifting in over-mining phase without effective gain

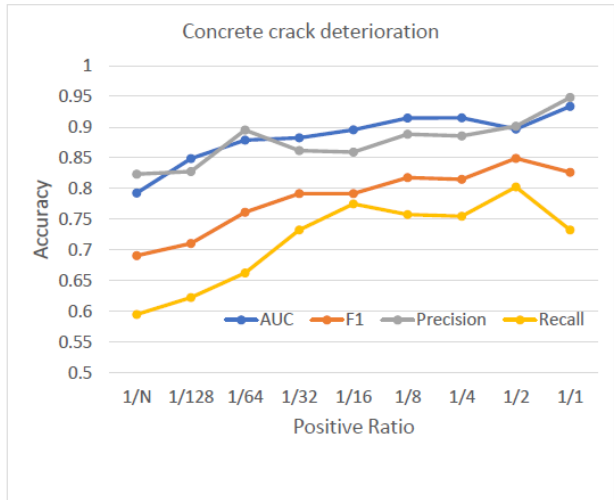


Figure 20. Anomalous vision mining studies on concrete crack, indicates that the more anomalies of damage vision, the higher performance of anomaly detection.

of accuracy. The former phase of damage vision mining opportunities has become beneficial because of advantage of higher accuracy in terms of the AUC.

3.7. River sludge

3.7.1 Backbone Studies of Supervised Detection

As shown in Table 13, our deeper FCDD-ResNet101 outperformed in terms of the F_1 , precision, and recall rather than the baseline CNN27 and other backbone-based deeper FCDDs in this river surface images dataset for detecting river sludge floating on the surface.

Table 13. Backbone ablation studies on river sludge detection using our proposed deeper FCDDs.

Backbone	AUC	F_1	Precision	Recall
CNN27	0.9518	0.8567	0.8940	0.8225
VGG16	0.9666	0.9065	0.9291	0.8850
ResNet101	0.9681	0.9214	0.9496	0.8950
InceptionV3	0.9623	0.9010	0.9402	0.8650

3.7.2 Imbalanced-to-unsupervised Training Results

As shown in Table 14, we implemented ablation studies on imbalanced data that contains smaller anomalous images and relatively large normal images. Herein, we applied our deeper FCDD-ResNet101 achieved high performance in the aforementioned supervised results. Compared with the balanced case of positive ratio 1/1, we found that there was applicable range from the imbalanced ratio 1/2 to the ratio 1/4 where the accuracy of F_1 was consistently more than 90%. However, extremely imbalanced range from 1/8 to 1/1300,

that accuracy were inferior to those of applicable range. The positive ratio 1/8 represent the imbalanced data that contains 163 anomalous images and relatively large 1300 normal images. In the situation, much more anomalous images should be acquired and added to the initial dataset. The marginal gain of accuracy was relatively high by adding the river sludge images on the surface.

Table 14. Imbalanced data studies using our deeper FCDD-ResNet101 for River sludge detection $N_6 = 1300$.

Positive ratio	AUC	F_1	Precision	Recall
1/1(ano. N_6)	0.9681	0.9214	0.9496	0.8950
1/2(ano.650)	0.9635	0.9175	0.9468	0.8900
1/4(ano.325)	0.9457	0.9077	0.8934	0.9225
1/8(ano.163)	0.9588	0.8736	0.9222	0.8300
1/16(ano.81)	0.9428	0.8579	0.9150	0.8075
1/32(ano.41)	0.9267	0.8382	0.8686	0.8100
1/64(ano.20)	0.9131	0.8175	0.8746	0.7675
1/128(ano.10)	0.9123	0.7973	0.8676	0.7375
1/N_6(ano.1)	0.8221	0.7139	0.7513	0.6800

3.7.3 Damage-mark Heatmaps on River Sludge

We visualized the damage features by using Gaussian up-sampling in our deeper FCDD-ResNet101 network. Additionally, we generated a histogram of the anomaly scores of the test images in the imbalanced case with positive ratio 1/4. In Fig. 21, a damage-mark explanation is represented. The red region in the heatmap represents the river sludge of features in the river surface images. Fig. 22 illustrates that a few overlapping bins exist in the boundary of the normal class and river sludge class along the horizontal anomaly scores. Thus, for detecting river sludge on the surface, the score range was well separated in the river sludge images dataset.

3.7.4 Effect on Damage Class Mining

As shown in Figure 23, from the view point of all accuracy, the imbalanced studies on river sludge implied that all of accuracy were consistently converged into significant phases. Ranged with the positive ratio less than 1/8, we could understand that there were damage vision mining opportunities with accuracy gain in terms of the AUC. In contrast, ranged with positive ratio over 1/4, it was shifting in over-mining phase without any gain of the AUC. The former phase of damage vision mining opportunities has become beneficial because of promising advantage of higher accuracy in all of them.

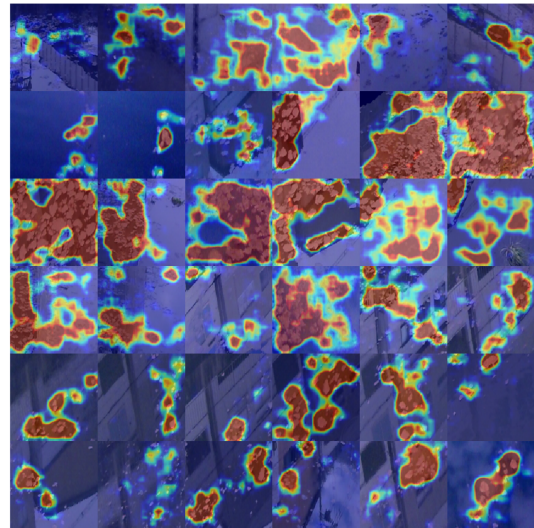


Figure 21. Imbalanced damage images (top) with positive ratio 1/4, and damage-mark heatmaps (bottom) of river sludge using our deeper FCDD-ResNet101.

3.8. Disaster Damage

3.8.1 Backbone Studies of Supervised Detection

As shown in Table 15, our deeper FCDD-VGG16 outperformed in terms of the AUC, F_1 , and precision, rather than the baseline CNN27 and other backbone-based deeper FCDDs in this disaster damage dataset for detecting building collapse, traffic incidents, fire, and flooding area.

3.8.2 Imbalanced-to-unsupervised Training Results

As shown in Table 16, we implemented ablation studies on imbalanced data that contains smaller anomalous images

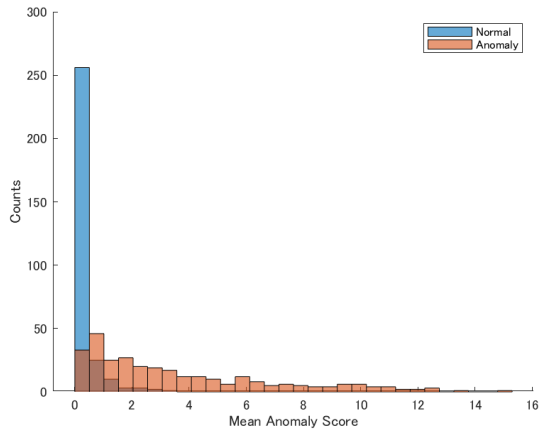


Figure 22. Histogram of river sludge scores using our deeper FCDD-ResNet101 corresponding to the imbalanced damage images with positive ratio 1/4.

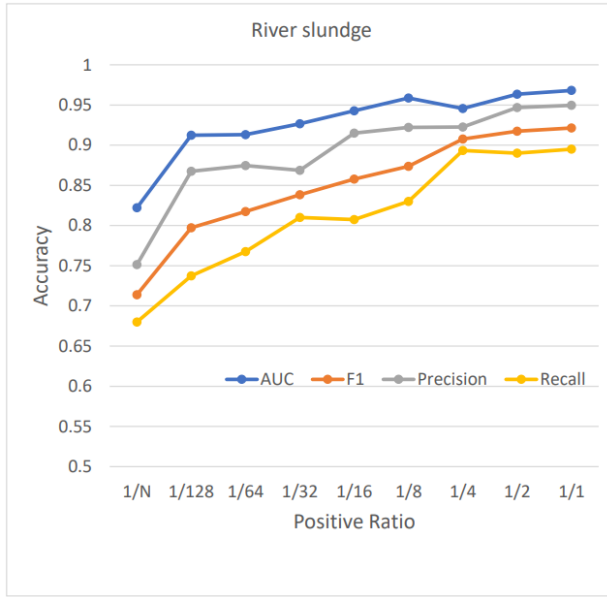


Figure 23. Anomalous vision mining studies on river sludge, indicates that the more anomalies of damage vision, the higher performance of anomaly detection.

Table 15. Backbone ablation studies on disaster damage detection using our proposed deeper FCDDs.

Backbone	AUC	<i>F</i> ₁	Precision	Recall
CNN27	0.9433	0.7896	0.7523	0.8307
VGG16	0.9969	0.9622	0.9589	0.9655
ResNet101	0.9916	0.9323	0.8985	0.9687
Inceptionv3	0.9925	0.9319	0.9189	0.9453

and relatively large normal images. Herein, we applied our deeper FCDD-VGG16 achieved high performance in the aforementioned supervised results. Compared with the bal-

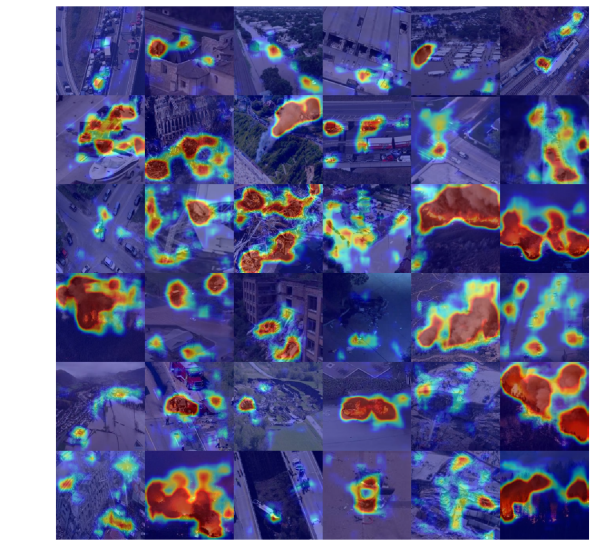


Figure 24. Imbalanced damage images (top) with positive ratio 1/16, and damage-mark heatmaps (bottom) of disaster damage using our deeper FCDD-VGG16.

anced case of positive ratio 1/1, we found that there was applicable range from the imbalanced ratio 1/2 to the ratio 1/16 where the accuracy were consistently high performance. However, extremely imbalanced range from 1/32 to 1/1300, that accuracy were inferior to those of applicable range. The rare positive ratio 1/32 represent the imbalanced data that contains quite a little 41 anomalous images and relatively large 1300 normal images. In the situation, much more anomalous images should be acquired and added to the initial dataset. The marginal gain of accuracy was relatively high by adding the rare events of devastated images.

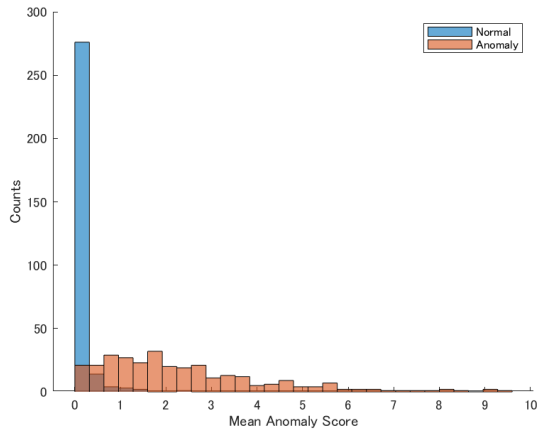


Figure 25. Histogram of disaster damage scores using our deeper FCDD-VGG16 corresponding to the imbalanced damage images with positive ratio 1/16.

Table 16. Imbalanced data studies using our deeper FCDD-VGG16 for Disaster damage detection $N_7 = 1300$.

Positive ratio	AUC	F_1	Precision	Recall
1/1(ano. N_7)	0.9844	0.9491	0.9410	0.9575
1/2(ano.650)	0.9850	0.9398	0.9422	0.9375
1/4(ano.325)	0.9843	0.9422	0.9469	0.9375
1/8(ano.163)	0.9809	0.9423	0.9447	0.9400
1/16(ano.81)	0.9766	0.9413	0.9401	0.9425
1/32(ano.41)	0.9606	0.9075	0.9075	0.9075
1/64(ano.20)	0.9444	0.8924	0.8826	0.9025
1/128(ano.10)	0.8971	0.8221	0.8484	0.7975
1/N_7(ano.1)	0.6870	0.5783	0.6721	0.5075

3.8.3 Damage-mark Heatmaps on Disaster Damage

We visualized the damage features by using Gaussian up-sampling in our deeper FCDD-VGG16 network. Additionally, we generated a histogram of the anomaly scores of the test images in the imbalanced case with positive ratio 1/16. In Fig. 24, a damage-mark explanation is represented. The red region in the heatmap represents the four classes of disaster features that includes fire and smoke, building collapse, traffic incidents, and flooding area. Fig. 25 illustrates that a few overlapping bins exist in the boundary of the ordinary class and disaster class along the horizontal anomaly scores. Thus, for detecting devastated feature, the score range was well separated in the disaster damage dataset.

3.8.4 Effect on Damage Class Mining

As shown in Figure 26, from the view point of all accuracy, the imbalanced studies on disaster damage implied that all of accuracy were consistently converged into significant phases. Ranged with the positive ratio less than 1/8, we could understand that there were damage vision mining

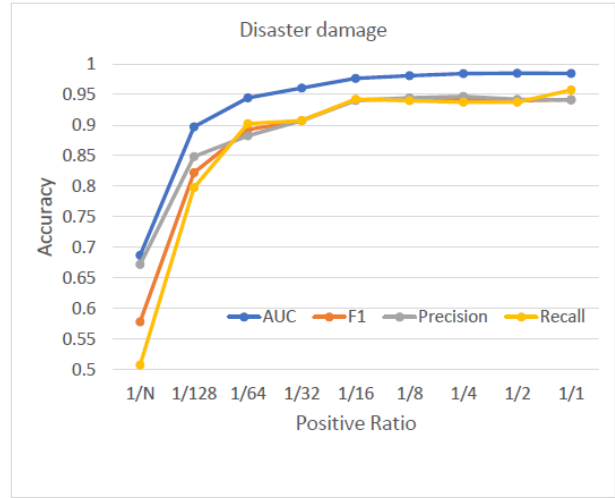


Figure 26. Anomalous vision mining studies on disaster damage, indicates that the more anomalies of damage vision, the higher performance of anomaly detection.

opportunities with accuracy gain. In contrast, ranged with positive ratio over 1/4, it was shifting in over-mining phase without any gain of accuracy. The former phase of damage vision mining opportunities has become beneficial because of promising advantage of higher accuracy in all of them.

3.9. Hurricane damage

3.9.1 Backbone Studies of Supervised Detection

As shown in Table 17, our deeper FCDD-ResNet101 outperformed in terms of the F_1 , and recall rather than the baseline CNN27 and other backbone-based deeper FCDDs in this satellite imagery dataset by remote sensing for detecting hurricane damage.

Table 17. Backbone ablation studies on hurricane damage detection using our proposed deeper FCDDs.

Backbone	AUC	F_1	Precision	Recall
CNN27	0.9858	0.9297	0.9172	0.9425
VGG16	0.9980	0.9671	0.9770	0.9575
ResNet101	0.9982	0.9753	0.9611	0.9900
Inceptionv3	0.9979	0.9623	0.9671	0.9575

3.9.2 Imbalanced-to-unsupervised Training Results

As shown in Table 18, we implemented ablation studies on imbalanced data that contains smaller anomalous images and relatively large normal images. Herein, we applied our deeper FCDD-ResNet101 achieved high performance in the aforementioned supervised results. Compared with the balanced case of positive ratio 1/1, we found that there was applicable range from the imbalanced ratio 1/2 to the ratio 1/16 where the accuracy of recall was consistently more

than 97%. However, extremely imbalanced range from 1/32 to 1/1300, that accuracy were inferior to those of applicable range. The rare positive ratio 1/32 represent the imbalanced data that contains quite a little 41 anomalous images and relatively large 1300 normal images. In the situation, much more anomalous images should be acquired and added to the initial dataset. The marginal gain of accuracy was relatively high by adding the remote sensing of hurricane damage satellite imagery.

Table 18. Imbalanced data studies using our deeper FCDD-ResNet101 for Hurricane damage detection $N_8 = 1300$.

Positive ratio	AUC	F_1	Precision	Recall
1/1(ano. N_8)	0.9982	0.9753	0.9611	0.9900
1/2(ano.650)	0.9986	0.9851	0.9754	0.9950
1/4(ano.325)	0.9981	0.9739	0.9656	0.9825
1/8(ano.163)	0.9956	0.9558	0.9375	0.9750
1/16(ano.81)	0.9962	0.9641	0.9535	0.9750
1/32(ano.41)	0.9889	0.9564	0.9815	0.9325
1/64(ano.20)	0.9818	0.9420	0.9492	0.9350
1/128(ano.10)	0.9734	0.9324	0.9702	0.8975
1/N_8(ano.1)	0.8155	0.7376	0.6807	0.8050

3.9.3 Damage-mark Heatmaps on Hurricane Damage

We visualized the damage features by using Gaussian up-sampling in our deeper FCDD-ResNet101 network. Additionally, we generated a histogram of the anomaly scores of the test images in the imbalanced case with positive ratio 1/16. In Fig. 27, a damage-mark explanation is represented. The red region in the heatmap represents the hurricane damage of flooding features in the remote sensing satellite imagery. Fig. 28 illustrates that a few overlapping bins exist in the boundary of the normal class and hurricane damaged class along the horizontal anomaly scores. Thus, for detecting hurricane damage of the flooding feature, the score range was well separated in the remote sensing satellite imagery dataset.

3.9.4 Effect on Damage Class Mining

As shown in Figure 29, from the view point of all accuracy, the imbalanced studies on hurricane damage implied that all of accuracy were consistently converged into significant phases. Ranged with the positive ratio less than 1/32, we could understand that there were damage vision mining opportunities with accuracy gain in terms of the AUC. In contrast, ranged with positive ratio over 1/16, it was shifting in over-mining phase without any gain of the AUC. The former phase of damage vision mining opportunities has become beneficial because of promising advantage of higher accuracy in all of them.

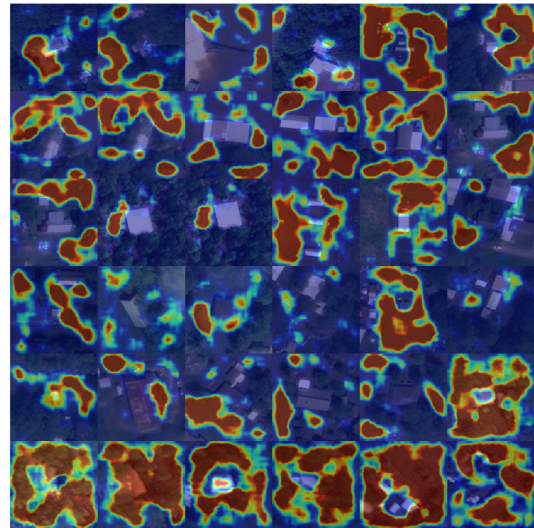


Figure 27. Imbalanced damage images (top) with positive ratio 1/16, and damage-mark heatmaps (bottom) of hurricane damage using our deeper FCDD-ResNet101.

4. Concluding Remarks

4.1. Anomaly Detection for Class Imbalance

We developed an imbalanced vision application to automate one-class anomaly detection. To ensure feasibility of imbalanced damage vision datasets on the targets of blood infection, wooden/concrete deterioration, and disaster damage. We assessed imbalanced anomaly detection approach for deeper FCDDs with a significant backbone of ResNet101 for the blood and lung infection, river sludge, and hurricane damage. Furthermore, we found that imbalanced anomaly detection method for deeper FCDDs with

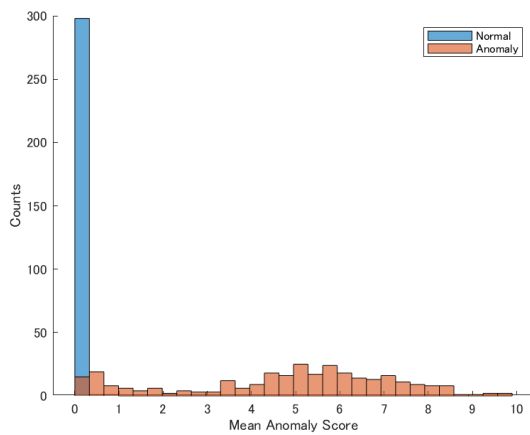


Figure 28. Histogram of hurricane damage scores using our deeper FCDD-ResNet101 corresponding to the imbalanced damage images with positive ratio 1/16.

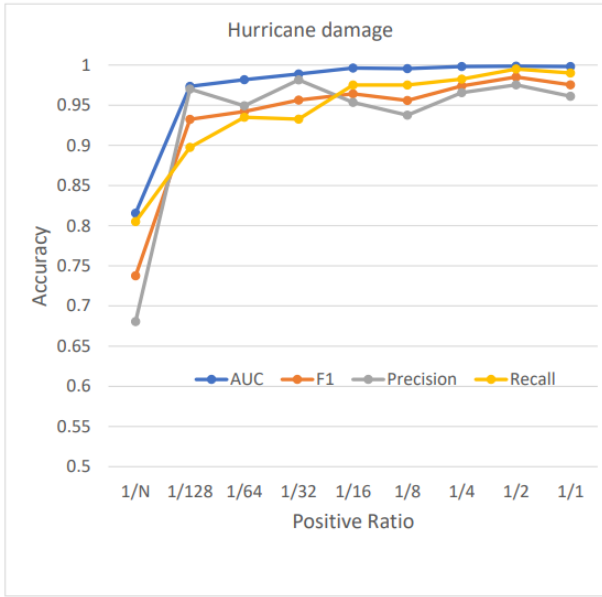


Figure 29. Anomalous vision mining studies on hurricane damage, indicates that the more anomalies of damage vision, the higher performance of anomaly detection.

a promising backbone of VGG16 for the wooden and concrete deterioration, and disaster damages. Additionally, we visualized damage-mark heatmaps using direct Gaussian upsampling of the receptive field of the FCN.

Our experiments produced significantly high accuracy in terms of the AUC, F_1 , precision, and recall using our deeper FCDDs architecture under the imbalanced datasets with relatively small positive ratio. That created the damage-mark heatmap for visual explanation, even without annotating the target of damage at the localized regions. In our imbalanced studies, compared with the balanced case of positive ratio

1/1, we found that there was applicable positive ratio 1/8, where the accuracy were consistently high. However, extremely imbalanced range from 1/128 to 1/16, whose accuracy were inferior to those of applicable ratio. In contrast, ranged with positive ratio over 1/4, it was shifting in over-mining phase without effective gain of accuracy. Thus, our imbalanced studies presented an applicability for deeper FCDDs that offers an imbalanced damage detection tool for damage-explainability.

4.2. Limitation and Robustness for Unseen Damage

This study discovered the feasibility of imbalanced anomaly detection highlighting limited targets using the specific available datasets in the present. Exactly, open feature still remains for practical use in each domain. For example, medical disease images, material deterioration, natural disaster damage, water environmental damage, earth surface damage. In outdoor field, we should consider temperature variation of damage vision in the background, e.g. winter season may influence the unseen background noise: shadow in sunset, decayed grass, iced, and snowy.

Several promising directions exist for future research to improve the usability of damage vision applications. The damage vision mining in imbalanced rare events would take longer time for becoming stable accuracy. To overcome this hurdle, the anomaly score can be used in edge devices for effective data acquisition of rare classes. By unseen data mining only the anomalous vision that have damage-marks with significantly higher anomaly scores than a particular threshold, the data acquisition process can be made more efficient.

From our key results of imbalanced studies, we found that the positive ratio of over 1/128 to 1/8 brought a promising accuracy gain as a damage vision mining merit. In contrast, ranging with the positive ratio over 1/4, the accuracy has not been further gained effectively. This implies that over-mining phase has not been beneficial that we should early stop the over-mining phase of further data acquisition.

We are going to tackle the opportunities of unseen damage vision mining and improving the robustness of damage detection applications to overcome the combination of imbalance type in damage vision, based on our initial studies on flood inflow using regression[43, 46], typhoon damage and river scum using image classification[42, 44], construction material condition clustering using contrastive metric learning[49], concrete exfoliation and snow covered road using semantic segmentation[40, 41, 48, 51], and earthquake disaster and bridge slab deterioration using anomaly detection[39, 45, 47].

Acknowledgment

The authors wish to thank MathWorks and Computer Vision Toolbox Team, Takuji Fukumoto for providing helpful MATLAB resources for Automated Visual Inspection. We also thank Nakasha Creative Co.,Ltd., for the opportunity of damage vision study.

References

- [1] S. Agarwal, J. O. D. Terrail, and F. Jurie. Recent advances in object detection in the age of deep convolutional neural networks, 2018. [2](#) [3](#)
- [2] Yancheng Bai and Bernard Ghanem. Multi-scale fully convolutional network for face detection in the wild. *Computer Vision and Pattern Recognition (CVPR)*, page 132–141, 2017. [2](#)
- [3] G. E. Batista, R. C. Prati, and M. C. Monard. A study of the behavior of several methods for balancing machine learning training data. *ACM SIGKDD explorations newsletter*, 6(1):20–29, 2004. [2](#)
- [4] Quoc Dung Cao and Youngjun Choe. Building damage annotation on post-hurricane satellite imagery based on convolutional neural networks, 2018. [5](#)
- [5] Quoc Dung Cao and Youngjun Choe. Detecting damaged buildings on post-hurricane satellite imagery based on customized convolutional neural networks. *IEEE Dataport*: <https://dx.doi.org/10.21227/sdad-1e56>, (accessed on 7 August 2023). [5](#)
- [6] H.-Y. Chen, P.-H. Wang, C.-H. Liu, S.-C. Chang, J.-Y. Pan, Y.-T. Chen, W. Wei, and D.-C. Juan. Complement objective training. *International Conference on Learning Representation (ICLR)*, 2019. [2](#) [3](#)
- [7] Narayana Darapaneni, Naman Vig, Anwesh Reddy Paduri, Jai Arora, Simrandeep Singh Gandhi, MoniShankar Hazra, and Saurabh Gupta. Detection of distracted driver using convolution neural network, 2022. [5](#)
- [8] P. Dollar, C. Wojek, B. Schiele, and P. Perona. Pedestrian detection: An evaluation of the state of the art. *IEEE Transactions on Pattern Analysis and Machine Intelligence (TPAMI)*, 34(4):743–761, 2012. [2](#)
- [9] S. Dorafshan, R.J. Thomas, and M. Maguire. SDNET2018: An annotated image dataset for noncontact concrete crack. *Data in Brief*, 21:1664–1668, 2018. [5](#)
- [10] Y. g. Kim, Y. Kwon, and M. C. Paik. Valid oversampling schemes to handle imbalance. *Pattern Recognition Letters*, 125:661–667, 2019. [2](#) [3](#)
- [11] Kaggle. COVID-19 Radiography Database. Available online: <https://www.kaggle.com/tawsifurrahman/covid19-radiographydatabase>, (accessed on 3 August 2023). [2](#) [5](#)
- [12] Kaggle. State Farm Distracted Driver Detection. Available online: <https://www.kaggle.com/c/state-farm-distracted-driver-detection/data>, (accessed on 7 August 2023). [5](#)
- [13] Bingyi Kang, Saining Xie, Marcus Rohrbach, Zhicheng Yan, Albert Gordo, Jiashi Feng, and Yannis Kalantidis. Decoupling representation and classifier for long-tailed recognition. *International Conference on Learning Representation (ICLR)*, 2020. [3](#)
- [14] Ejaz Khan, Muhammad Zia Ur Rehman, Fawad Ahmed, Faisal Abdulaziz Alfouzan, Nouf M. Alzahrani, and Jawad Ahmad. Chest X-ray classification for the detection of COVID-19 using deep learning techniques. *Sensors*, 22(1211), 2022. [2](#) [5](#)
- [15] Stefanus Tao Hwa Kieu, Abdullah Bade, Mohd Hanafi Ahmad Hijazi, and Hoshang Kolivand. A survey of deep learning for lung disease detection on medical images: State-of-the-art, taxonomy, issues and future directions. *Journal of Imaging*, 6(131), 2020. [2](#)
- [16] Yechan Kim, Younkwon Lee, and Moongu Jeon. Imbalanced image classification with complement cross entropy, 2020. [2](#)
- [17] M. Kozierski. Radial-based undersampling for imbalanced data classification. *Pattern Recognition*, 102:107262, 2020. [2](#) [3](#)
- [18] C. Kyrkou and T. Theocharides. Deep-learning-based aerial image classification for emergency response applications using unmanned aerial vehicles. *Workshop on Computer Vision for UAVs CVPR*, 2019. [5](#)
- [19] Tianhong Li, Peng Cao, Yuan Yuan, Lijie Fan, Yuzhe Yang, Rogerio S Feris, Piotr Indyk, and Dina Katabi. Targeted supervised contrastive learning for long-tailed recognition. *Computer Vision and Pattern Recognition (CVPR)*, page 6918–6928, 2022. [3](#)
- [20] T.-Y. Lin, P. Goyal, R. Girshick, K. He, and P. Dollár. Focal loss for dense object detection. *International Conference on Computer Vision (ICCV)*, 32(10):2980–2988, 2017. [2](#) [3](#)
- [21] G. Litjens, T. Kooi, B. E. Bejnordi, A. A. A. Setio, F. Ciompi, M. Ghafoorian, J. A. van der Laak, B. van Ginneken, and C. I. Sánchez. A survey on deep learning in medical image analysis. *Medical Image Analysis*, 42:60–88, 2017. [2](#)
- [22] Philipp Liznerski, Lukas Ruff, Robert A. Vandermeulen, Billy Joe Franks, Marius Kloft, and Klaus-Robert Müller. Explainable deep one-class classification. In *The International Conference on Learning Representations (ICLR)*, Workshop on Uncertainty and Robustness in Deep Learning, 2021. [4](#)
- [23] Aditya Krishna Menon, Sadeep Jayasumana, Ankit Singh Rawat, Himanshu Jain, Andreas Veit, and Sanjiv Kumar. Long-tail learning via logit adjustment. *International Conference on Learning Representation (ICLR)*, 2020. [3](#)
- [24] Kemal Oksuz, Baris Can Cam, Sinan Kalkanz, and Emre Akbas. Imbalance problems in object detection: A review, 2020. [2](#) [3](#)
- [25] Vardan Papyan, XY Han, and David L Donoho. Prevalence of neural collapse during the terminal phase of deep learning training. *Proceedings of the National Academy of Sciences*, 117(40):24652–24663, 2020. [3](#)
- [26] L. Piras and G. Giacinto. Synthetic pattern generation for imbalanced learning in image retrieval. *Pattern Recognition Letters*, 33(16):2198–2205, 2012. [2](#)
- [27] Sivaramakrishnan Rajaraman, Sameer K. Antani, Mahdieh Poostchi, Kamolrat Silamut, Md. A. Hossain, Richard J. Maude, Stefan Jaeger, and George R. Thoma. Pre-trained convolutional neural networks as feature extractors toward improved malaria parasite detection in thin blood smear images. *PeerJ*, 6:e4568, 2018. [5](#)

[28] Jiawei Ren, Cunjun Yu, Shunan Sheng, Xiao Ma, Haiyu Zhao, Shuai Yi, and Hongsheng Li. Balanced softmax for long-tailed visual recognition. *NeurIPS*, page 4175–4186, 2020. 3

[29] Marco Tulio Ribeiro, Sameer Singh, and Carlos Guestrin. “why should i trust you?”: Explaining the predictions of any classifier. In *Proceedings of the 22nd ACM SIGKDD International Conference on Knowledge Discovery and Data Mining*, KDD ’16, page 1135–1144. Association for Computing Machinery, 2016. 4

[30] Lukas Ruff, Robert A. Vandermeulen, Billy Joe Franks, Klaus-Robert Müller, and Marius Kloft. Rethinking assumptions in deep anomaly detection. In *The International Conference on Machine Learning (ICML)*, Workshop on Uncertainty and Robustness in Deep Learning, 2021. 4

[31] Ramprasaath R. Selvaraju, Michael Cogswell, Abhishek Das, Ramakrishna Vedantam, Devi Parikh, and Dhruv Batra. Grad-CAM: Visual explanations from deep networks via gradient-based localization. In *2017 IEEE International Conference on Computer Vision (ICCV)*, pages 618–626, 2017. 4

[32] Samuel Stocksieber, Denys Pommeret, and Arthur Charpentier. Data augmentation for imbalanced regression, 2023. 2, 3

[33] Zehang Sun, G. Bebis, and R. Miller. On-road vehicle detection: a review. *IEEE Transactions on Pattern Analysis and Machine Intelligence (TPAMI)*, 28(5):694–711, 2006. 2

[34] Christos Thrampoulidis, Ganesh R Kini, Vala Vakilian, and Tina Behnia. Imbalance trouble: Revisiting neural-collapse geometry, 2022. 3

[35] C. Wang, C. Deng, and S. Wang. Imbalance-xgboost: leveraging weighted and focal losses for binary label-imbalanced classification with xgboost. *Pattern Recognition Letters*, 2020. 2, 3

[36] Liang Xie, Yibo Yang, Deng Cai, and Xiaofei He. Neural collapse inspired attraction-repulsion-balanced loss for imbalanced learning, 2022. 3

[37] Yibo Yang, Liang Xie, Shixiang Chen, Xiangtai Li, Zhouchen Lin, and Dacheng Tao. Do we really need a learnable classifier at the end of deep neural network? *NeurIPS*, 2022. 3

[38] Yuzhe Yang, Kaiwen Zha, Ying-Cong Chen, Hao Wang, and Dina Katabi. Delving into deep imbalanced regression. In *Proceedings of the 38th International Conference on Machine Learning (ICML)*, PMLR 139, 2021. 1, 3

[39] T. Yasuno. Color base damage feature enhanced support vector classifier for monitoring quake image. In *International Workshop on Computational Color Imaging (CCIW)*, Chiba, 2019. 18

[40] T. Yasuno. Popouts segmentation for concrete prognosis indices using uav monitoring and dense dilated convolutions. In *Proceeding of International Workshop on Structural Health Monitoring (IWSHM)*, Stanford University, CA, 2019. 18

[41] Takato Yasuno. Generative synthetic augmentation using edge-detected semantic labels for segmentation accuracy, 2020. 18

[42] T. Yasuno. Natural disaster classification using aerial photography explainable for typhoon damaged feature. In *The International Conference on Pattern Recognition (ICPR)*, Workshop on Machine Learning Advances Environmental Science (MAES), 2020. 18

[43] T . Yasuno, M. Amakata, and J. Fujii. L2 norm ensemble regression with ocean feature weights by analyzed images for flood inflow forecast, 2021. 18

[44] T. Yasuno, J. Fujii, and M. Amakata. River surface patch wise detector using mixture augmentation for scum cover index. In *International Conference on Computer Vision(ICCV)*, Vancouver, 2022. 5, 18

[45] T. Yasuno, J. Fujii, and M. Nakajima. Bridge slab anomaly detector using U-Net generator with patch discriminator for robust prognosis. In *Structural Health Monitoring, Proceeding of International Workshop on Structural Health Monitoring (IWSHM)*, Stanford University, CA, 2021. 18

[46] T. Yasuno, A. Ishii, and M. Amakata. Rain code : Multi frame based spatiotemporal precipitation using ConvLSTM. In *The International Conference on Pattern Recognition (ICPR)*, Workshop on Pattern Forecasting (PATCAST), 2020. 18

[47] T. Yasuno, A. Ishii, J. Fujii, and A. Masazumi. Generative damage learning for concrete aging detection using auto flight images. In *The International Symposium on Automation and Robotics in Construction (ISARC)*, 2020. 18

[48] T. Yasuno, M. Nakajima, and K . Noda. Per pixel classification rebar exposures in bridge eye inspection, 2020. 18

[49] T. Yasuno, M. Okano, and J. Fujii. MN pair contrastive damage representation and clustering for prognostic explanation. In *The International Symposium on Automation and Robotics in Construction (ISARC)*, Workshop on, 2023. 18

[50] Takato Yasuno, Masahiro Okano, and Junichiro Fujii. One-class damage detector using deeper fully convolutional data descriptions for civil application. *Advances in Artificial Intelligence and Machine Learning*, 3(2):996–1011, 2023. 4

[51] T. Yasuno, H. Sugawara, and J. Fujii. Road surface translation under snow covered and semantic segmentation for snow hazard index. In *Advances in Artificial intelligence Selected Papers from the Annual Conference of JSAI2021*, Springer, 2021. 18

[52] S. Zafeiriou, C. Zhang, and Z. Zhang. A survey on face detection in the wild. *Computer Vision and Image Understanding*, 138:1–24, 2015. 2

[53] Matthew D Zeiler and Rob Fergus. Visualizing and understanding convolutional networks, 2013. 4

[54] Zhisheng Zhong, Jiequan Cui, Shu Liu, and Jiaya Jia. Improving calibration for long-tailed recognition. *Computer Vision and Pattern Recognition (CVPR)*, page 16489–16498, 2021. 3

[55] Zhisheng Zhong, Jiequan Cui, Yibo Yang, Xiaoyang Wu, Xiaojuan Qi, Xiangyu Zhang, and Jiaya Jia. Understanding imbalanced semantic segmentation through neural collapse, 2023. 3

[56] Bolei Zhou, Aditya Khosla, Agata Lapedriza, Aude Oliva, and Antonio Torralba. Learning deep features for discriminative localization, 2015. 4

- [57] Jianggang Zhu, Zheng Wang, Jingjing Chen, Yi-Ping Phoebe Chen, and Yu-Gang Jiang. Balanced contrastive learning for long-tailed visual recognition. *Computer Vision and Pattern Recognition (CVPR)*, page 6908–6917, 2022. [3](#)
- [58] Y. Zhu, C. Jia, F. Li, and J. Song. Inspector: a lysine succinylation predictor based on edited nearest-neighbor undersampling and adaptive synthetic oversampling. *Analytical Biochemistry*, 593:113592, 2020. [2](#)
- [59] Z. Zou, Z. Shi, Y. Guo, and J. Ye. Object detection in 20 years: A survey, 2018. [2](#), [3](#)